AIAA JOURNAL
Vol. 47, No. 4, April 2009

Multiproperty Measurements at High Sampling Rates Using Rayleigh Scattering

Amy F. Mielke*
NASA John H. Glenn Research Center at Lewis Field, Cleveland, Ohio 44135
Kristie A. Elam†
Jacobs Sverdrup, Cleveland, Ohio 44135
and
Chih-Jen Sung‡
Case Western Reserve University, Cleveland, Ohio 44106

DOI: 10.2514/1.37369

A molecular Rayleigh scattering technique is developed to measure gas velocity, temperature, and density in unseeded gas flows at sampling rates up to 32 kHz. A high-power continuous-wave laser beam is focused at a point in an air flowfield, and Rayleigh scattered light is collected and fiber-optically transmitted to a Fabry–Perot interferometer for spectral analysis. Photomultiplier tubes operated in the photon-counting mode allow high-frequency sampling of the total signal level and the circular interference pattern to provide density, temperature, and velocity measurements. Mean and root-mean-square fluctuation measurements in both an electrically heated jet facility with a 10-mm-diam nozzle and in a hydrogen-combustor-heated-jet facility with a 50.8-mm-diam nozzle at NASA John H. Glenn Research Center at Lewis Field are presented. Measurements are compared with hot-wire anemometry, cold-wire thermometry, and temporally resolved particle image velocimetry to validate the Rayleigh technique.

Nomenclature

a = most probable molecular speed, $m \cdot s^{-1}$
c = speed of light, 2.998×10^8 $m \cdot s^{-1}$
D = nozzle exit diameter, m
d = Fabry–Perot mirror spacing, m
$\mathbf{E}$ = incident electric field vector, $V \cdot m^{-1}$
F = Fabry–Perot instrument function contrast
f_C = collimating-lens focal length, m
f_L = fringe-forming-lens focal length, m
f_s = sampling rate, s^{-1}
h = Planck's constant, 6.626×10^{-34} $N \cdot m \cdot s$
I_{FP} = Fabry–Perot instrument function
$\mathbf{K}$ = interaction wave vector, m^{-1}
K = magnitude of $\mathbf{K}$, m^{-1}
$\mathbf{k_0}$ = incident-light wave vector, m^{-1}
$\mathbf{k_s}$ = scattered-light wave vector, m^{-1}
L = length of subrecords in spectral calculations
L_x = probe volume length, m
l_m = mean free path between molecular collisions, m
Ma = acoustic Mach number
m = molecular mass, kg
N_e = effective finesse
N_q = photoelectron counts in the qth annular region
N_R = Rayleigh scattering signal collected into solid angle Ω
n = molecular number density, m^{-3}
P_0 = power of the incident laser beam, $J \cdot s^{-1}$
p = static pressure, $N \cdot m^{-2}$
q = annular region number
r = radial position in the image plane, m
$r_{i,q}$ = inner radius of the qth annular region, m
r_j = radial position in the jet flowfield, m
r_{max} = fiber-face image radius, m
$r_{o,q}$ = outer radius of the qth annular region, m
r_R = fringe radius for the reference laser light, m
S_R = Rayleigh scattering spectrum
T = static temperature, K
T_{amb} = ambient temperature, K
T_j = jet exit static temperature, K
T' = root-mean-square temperature fluctuations, K
U_j = jet exit velocity, $m \cdot s^{-1}$
u = axial component of the velocity vector $\mathbf{v}$, $m \cdot s^{-1}$
u_k = measured-velocity component, $m \cdot s^{-1}$
u' = root-mean-square axial velocity fluctuations, $m \cdot s^{-1}$
$\mathbf{v}$ = velocity vector, $m \cdot s^{-1}$
x = axial position in the jet flowfield, m
x_f = nondimensionalized frequency
y = y parameter
β = angle between $\mathbf{E}$ and the scattering plane, rad
Δt = integration time, s
ε = optical system efficiency
η = dynamic viscosity, $N \cdot s \cdot m^{-2}$
θ = angle between the light ray incident on Fabry–Perot and the optical axis, rad
κ = Boltzmann's constant, 1.381×10^{-23} $J \cdot K^{-1}$
Λ = wavelength corresponding to wave vector $\mathbf{K}$, m
λ = illumination wavelength, m
μ = refractive index
ν = frequency of scattered light, s^{-1}
ν_0 = frequency of incident laser light, s^{-1}
ρ = gas density, $kg \cdot m^{-3}$
χ_s = scattering angle, rad

Presented as Paper 262 at the 46th AIAA Aerospace Sciences Meeting and Exhibit, Reno, NV, 7–10 January 2008; received 29 February 2008; accepted for publication 8 July 2008.

*Research Engineer, Optical Instrumentation and Nondestructive Evaluation Branch, 21000 Brookpark Road, Mail Stop 77-1. Member AIAA.
†Optics Technician.
‡Professor, Department of Mechanical and Aerospace Engineering. Associate Fellow AIAA.

ψ = phase change between successive reflections in planar Fabry–Perot
Ω = solid angle, sr

I. Introduction

CURRENTLY, nonintrusive temperature-measurement techniques available for use in turbulent-flow studies in which the local pressure is unknown are limited to sampling rates of less than a few kilohertz. There are also no techniques that can provide nonintrusive time-resolved measurements of gas temperature, velocity, and density simultaneously at rates beyond a couple of kilohertz. Conventional intrusive measurement devices such as resistance wires, pressure probes, and thermocouples are usually limited in spatial and temporal resolution, disturb the flow under study, and can be damaged by high pressure or temperature. The Rayleigh scattering technique presented is unique in that it provides simultaneous temperature, velocity, and density measurements at sampling rates up to 32 kHz. A high-power single-frequency continuous-wave (CW) laser beam is focused at a point in an air flowfield, and Rayleigh scattered light is collected and transmitted via optical fiber to another location at which the light is spectrally resolved. The signal strength and spectrum of the light contain information about the density, temperature, and velocity of the flow. A planar-mirror Fabry–Perot interferometer (FPI) is used to analyze the spectrum of the scattered light, and photomultiplier tubes (PMTs) record the signal strength and fringe-intensity pattern at high sampling rates, enabling time-resolved measurement of the gas-flow properties. The ability to obtain dynamic high-frequency-response measurements of multiple properties simultaneously is a valuable tool for compressible turbulent-flow research.

Dynamic flow measurements are particularly useful to aeroacoustics researchers who are interested in correlating flow property fluctuations with far-field acoustic fluctuations, leading to validation and improvement of computational aeroacoustics noise-prediction codes. Knowledge of velocity-temperature fluctuation correlations and turbulent Prandtl number are also needed to improve computational fluid dynamic (CFD) models of compressible turbulent flows. The ability to route the signal, and potentially the incident illumination, via fiber optics makes this technique appealing to facilities researchers who typically require flow measurements in harsh environments with tight space constraints.

Various optical techniques are available for temperature, molecular number density, and velocity measurements. Optical flow-measurement techniques can be divided into two basic categories:

1) Molecular-based techniques can involve elastic (non-energy-exchanging) or inelastic (energy-exchanging) scattering processes from atoms or molecules or absorption of light by molecules sometimes followed by spontaneous emission.

2) Particle-scattering techniques involve elastic scattering from particles (Mie scattering) entrained in the flow.

Molecular-based techniques are free of problems associated with the seeding of flows with particulates, such as abrasiveness to equipment and difficulties with achieving proper flow-seeding conditions. Because the gas-molecule properties are directly determined, molecular-based techniques are capable of providing gas temperature and density information not available in particle-based techniques.

Eckbreth [1] provides the details of several molecular-based techniques, such as coherent anti-Stokes Raman spectroscopy (CARS), spontaneous Raman and Rayleigh scattering, and laser induced fluorescence, with an emphasis on their use in combustion applications. Other molecular-based techniques include laser-induced gratings [2,3], filtered Rayleigh scattering [4], frequency-modulated filtered Rayleigh scattering [5,6], collective light scattering [7], molecular flow-tagging techniques [8], and tunable diode laser absorption spectroscopy [9]. The most common particle-based techniques are laser Doppler velocimetry [10], particle image velocimetry (PIV) [11], and planar Doppler velocimetry [12].

The temporal response of many optical measurement techniques is typically limited by the repetition rate of pulsed lasers. Advances in laser technology have led to recent demonstrations of temporally resolved PIV measurements in hot jets [11] and Rayleigh thermometry in flames [13] using pulsed lasers at rates exceeding 10 kHz. Although high-repetition-rate lasers exist, we take advantage of the stable frequency and narrow line width of solid-state diode-pumped CW laser systems in this work by collecting Rayleigh scattered light over a finite length of the high-power laser beam, spectrally filtering the light, and sampling the number of photons collected during very short integration periods. This arrangement provides pointwise multiproperty measurements with spatial resolution of approximately $0.1 \times 0.1 \times 1$ mm^3 at high temporal resolution without the need for multiple lasers and complex alignment requirements.

Previous works using molecular Rayleigh scattering to make temperature, velocity, and number density measurements in various environments [14–17] and dynamic density and velocity measurements in supersonic free jets [18,19] have been reported. Bivolaru et al. [20] developed a novel technique combining CARS and interferometric Rayleigh scattering to measure temperature, species concentration, and two components of velocity at low sampling rates in combusting flow environments. The Rayleigh technique described in this paper has been validated previously in an acoustically modulated nozzle flow and an asymmetric oscillating counterflow with unequal enthalpies; these modulated flows have been used to validate the velocity and temperature fluctuation measurements, respectively, by comparison with hot-wire and cold-wire probe measurements [21].

This paper describes the application of the technique for characterization of heated airflows. The first experiment studies the flow issuing from an electrically heated jet equipped with a 10-mm-diam nozzle that provides flow velocities up to 110 m/s and temperatures up to 775 K. The Rayleigh scattering measurements are compared with hot-wire and cold-wire measurements.

In response to NASA's mission to reduce aircraft noise levels, experiments have been conducted to evaluate the contribution of temperature fluctuations to far-field noise by application of the presented Rayleigh scattering technique in the small-hot-jet acoustic rig (SHJAR), which is a heated-nozzle facility located in the Aeroacoustic Propulsion Laboratory (AAPL) at the NASA John H. Glenn Research Center at Lewis Field (GRC). This facility can provide up to Mach 2 flow conditions with maximum temperatures approaching 970 K. Sound-pressure fluctuation (microphone) measurements will eventually be acquired simultaneously with Rayleigh measurements, allowing correlation between flow property fluctuations and noise generation.

Determining sources of jet noise will help engineers to design quieter, more efficient, aircraft. Data acquired in this facility at subsonic heated-flow conditions using a 50.8-mm-diam convergent nozzle are compared with temporally resolved PIV (TR-PIV) measurements. Although all three flow parameters (density, temperature, and velocity) have been measured in these two experiments, only velocity and temperature results are presented here because the density measurement has been demonstrated in previous work [19,22].

II. Theory

A. Rayleigh Scattering and Spectral Analysis

In molecular Rayleigh scattering, an incident electric field interacts with an atom or molecule, inducing a dipole moment that oscillates and radiates at the frequency of the incident field. It is considered an elastic scattering process because the internal energy of the molecule is unchanged. The frequency of the light is altered only by the Doppler effect due to the thermal as well as the bulk motion of the molecules. The frequency spectrum of the scattered light contains information about the gas density, bulk velocity, and temperature. Figure 1 shows a Rayleigh scattering spectrum containing the narrow laser line and a typical Rayleigh spectral peak to illustrate how the flow property measurements are obtained from

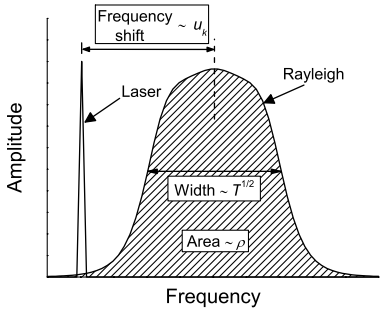

Fig. 1 Rayleigh scattering spectrum.

the spectral information. If the gas composition is fixed, the total intensity of the Rayleigh scattered light is directly proportional to the gas density. The frequency shift between the laser peak and the Rayleigh peak is proportional to the bulk flow velocity. The width of the spectrum is related to the gas temperature.

The shape of the spectrum is dependent on gas pressure p, temperature T, and scattering angle χ_s [23]. A nondimensional parameter y, which represents the ratio of the wavelength of the scattering grating ($\Lambda = \lambda/[2\sin(\chi_s/2)]$) to the mean free path between molecular collisions ($l_m = a\eta/n\kappa T$), is used to establish spectral shape regimes [24]:

$$y = \frac{\Lambda}{2\pi l_m} = \frac{p}{\eta K a} \tag{1}$$

where

$$a = \sqrt{\frac{2\kappa T}{m}} \tag{2}$$

The wavelength of the scattering grating is the wavelength associated with the interaction wave vector **K**, which defines the direction of the measured-velocity component u_k. **K** is the bisector of the incident- and scattered-light wave vectors (Fig. 2). The interaction wave vector and its magnitude are given by

$$\mathbf{K} = \mathbf{k_s} - \mathbf{k_0} \tag{3}$$

$$K = |\mathbf{K}| = \frac{4\pi}{\lambda}\left[\sin\frac{\chi_s}{2}\right] \tag{4}$$

The geometry of the optical arrangement in an experiment can be designed such that the desired component of the velocity vector **v** is measured:

$$u_k = \frac{\mathbf{K}\cdot\mathbf{v}}{K} \tag{5}$$

Experiments are typically arranged such that the electric field vector **E** is perpendicular to the scattering plane defined by the incident- and scattered-light wave vectors [$\beta = 90$ deg with s-type polarization (Fig. 2)]. In this situation, the collected scattering intensity is independent of the scattering angle and is maximized.

A kinetic theory model developed by Tenti et al. [23] and Boley et al. [25] (TENTI S6: 6-moment Rayleigh scattering model) provides the Rayleigh–Brillouin spectrum for diatomic gases and is incorporated in the model function used in maximum likelihood

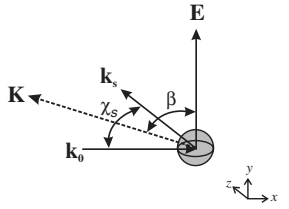

Fig. 2 Light scattering from a moving particle.

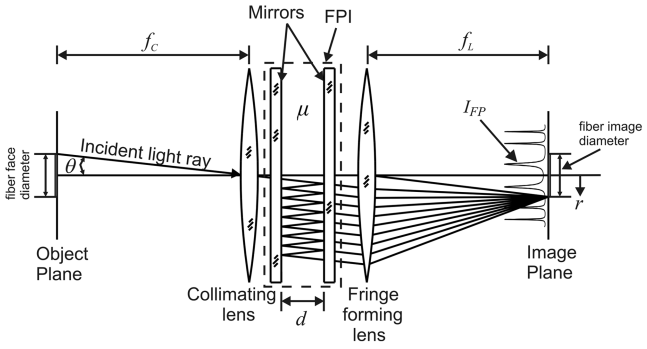

Fig. 3 Basic optical arrangement for spectrally analyzing a uniform light source using a planar-mirror Fabry–Perot interferometer.

estimation (MLE) analysis of the experimental data. This measurement technique requires spectral analysis of the Rayleigh scattered light. Figure 3 illustrates the basic arrangement for spectrally analyzing a uniform light source located at the focal plane of the collimating lens and imaged at the focal plane of the fringe-forming lens using a planar-mirror FPI [26]. The Fabry–Perot etalon consists of two parallel planar mirrors.

In this work, the FPI is operated in the static imaging mode in which the plate spacing d and medium refractive index μ are held constant, whereas the angle of the incoming light ray θ is varied by imaging points offaxis, which allows transmission of different frequencies to recreate the spectrum of the incident light. The lens at the etalon output images the light source at the image plane in which a detector is located. If the incoming light has a very narrow line width, the imaged intensity pattern is essentially a delta function convolved with the instrument function.

A one-dimensional representation of the instrument function I_{FP} is illustrated at the image plane in Fig. 3 for a single normalized-frequency value. A change in normalized frequency results in a physical shift of the fringe locations in the radial direction. For Rayleigh scattered light the resulting function at the image plane is the instrument function convolved with the Rayleigh spectrum. The line width of the broadened fringes provides a measure of temperature from Rayleigh scattered light. The frequency shift of the light associated with the bulk flow velocity is determined by a spatial shift in the fringe positions in the image.

In this work, the light source is a finite-diameter optical fiber face that is illustrated at the object plane in Fig. 3. The physical extent of the image of the fiber is also illustrated at the image plane. In this situation, the extent of the interference pattern that is detectable is limited by the image size, which is governed by the focal length of the imaging lenses. The physical extent of the fiber image in this work permitted imaging of the innermost fringe of the interference pattern only, as shown by the portion of the instrument function that falls within the extent of the image diameter in Fig. 3.

The fringe-intensity pattern is a function of both the Rayleigh spectrum and the Fabry–Perot instrument function. The Fabry–Perot instrument function in terms of normalized frequency x_f and radial position in the image plane r is given by the following relation:

$$I_{\mathrm{FP}}(x_f, r) = \frac{1}{1 + F\sin^2[\psi(x_f, r)/2]} \tag{6}$$

where

$$F = \frac{1}{\sin^2(\pi/2N_e)} \tag{7}$$

and the phase change between successive reflections is derived from Eq. 3 of [26] by applying the small-angle approximation and by expressing the absolute frequency ν as a function of normalized frequency:

$$\psi = \frac{4\pi\mu d}{\lambda}\left[1 + \frac{\lambda a}{c\Lambda}x_f\right]\left[1 - \frac{1}{2}\left(\frac{r}{f_L}\right)^2\right] \tag{8}$$

where the normalized frequency x_f is the ratio of the frequency change due to the bulk flow velocity and the frequency associated with the most probable molecular speed:

$$x_f = \frac{2\pi(\nu - \nu_0)}{Ka} \tag{9}$$

In this experiment, Rayleigh scattered light from a defined probe volume is collected into a multimode optical fiber. The incident laser beam is focused to a diameter smaller than the imaged field size, such that the power collected is proportional to the length of the probe volume set by the field size of the collection optics. The Rayleigh scattered light integrated over the collection solid angle Ω from a probe volume of length L_x expressed in terms of expected photoelectron counts is

$$\langle N_R \rangle = \int_{\Delta\Omega} \frac{\varepsilon P_0 n L_x \lambda \Delta t}{hc} \left(\frac{\partial\sigma}{\partial\Omega}\right) \sin^2\beta \partial\Omega \tag{10}$$

where the overall system efficiency ε includes detector quantum efficiency and other losses, and Δt is the integration time over which photoelectrons are counted. The differential scattering cross section $\partial\sigma/\partial\Omega$, and hence the scattering strength, scales with the fourth power of frequency; therefore, shorter wavelengths are desirable for Rayleigh scattering experiments.

The light exiting the fiber is collimated and directed to the FPI, and a lens at the interferometer output focuses the interference fringe pattern at the image plane. With the interferometer in the light path, the interference fringe pattern is equivalent to the intensity of the image of the fiber face without the Fabry–Perot modified by the transmission properties of the FPI. The circular interference pattern is split up into one circular and three annular regions, as shown in Fig. 4, and the light from each region is detected by four PMTs. The expected amount of energy collected from the qth annular region of the interference pattern in terms of photoelectron counts can be expressed by the following model function:

$$\langle N_q \rangle = \frac{\langle N_R \rangle}{\pi r_{\max}^2} 2\pi \int_{r_{i,q}}^{r_{o,q}} \int_{-\infty}^{\infty} S_R(x_f) I_{\mathrm{FP}}(x_f, r) r \, \mathrm{d}x_f \, \mathrm{d}r \tag{11}$$

where the Rayleigh spectrum S_R is evaluated using the TENTI S6 model. The developed model function given by Eq. (11) is used in MLE analysis of the experimental data.

The Fabry–Perot used in the experiments has a free spectral range, or frequency change between fringes, of 8.7 GHz and an effective finesse of approximately 15, which provides an instrument function width of 0.58 GHz. The width of the Rayleigh spectrum is set by the molecular thermal motion. For a temperature of 300 K, the Rayleigh spectral line width is approximately 1.1 GHz.

The extent of the imaged fringe pattern is limited by the lenses used to image the optical fiber face through the Fabry–Perot. The image diameter in the current experiments is equivalent to a partial fringe order, and therefore only the innermost fringe of the pattern is detectable. The outer diameter of the image is equivalent to approximately 0.4 times the free spectral range of the instrument, or a maximum frequency shift of approximately 3.5 GHz. This means that the maximum velocity that can be measured results in a frequency shift of less than this amount. The velocity associated with a 3.5 GHz frequency shift for the current experimental arrangement is 1300 m/s. This would require a reference fringe that is right at the edge of the image and a Doppler-shifted fringe at the origin of the concentric pattern. In reality, this would be an impossible situation to measure. A more realistic velocity measurement limit would be approximately half of this, or 650 m/s.

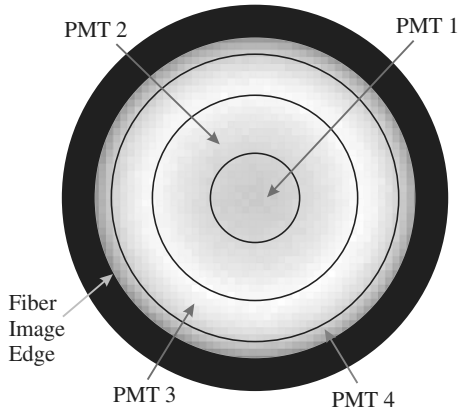

Fig. 4 Dissection of Fabry–Perot fringe pattern into one circular and three annular regions.

B. Lower Bound for Measurement Uncertainty

The lower bound on the uncertainty in temperature, velocity, and density measurements using Rayleigh scattering is set by the photon statistical (shot) noise. Shot noise can be modeled by a Poisson distribution. Estimates of the measurement uncertainty in the unknown parameters for the Rayleigh measurement technique are obtained by Cramer–Rao lower-bound (CRLB) analysis [27]. The results of this analysis were presented previously in [28,29]. The lower-bound uncertainty in the temperature, velocity, and density estimates acquired during a photon-counting integration period of 31.25 μs for air at a temperature of 298 K, standard atmospheric pressure, and mean velocity of 100 m/s for an instrument similar to the system used in these experiments with an overall system efficiency of approximately 2% is as follows:

$$\sigma_T \geq 58 \text{ K} \qquad \sigma_{u_k} \geq 30 \text{ m/s} \qquad \sigma_\rho \geq 0.78 \text{ kg/m}^3$$

The uncertainty in both temperature and velocity is inversely related to the square root of the number of photoelectron counts [28,29]; therefore, increasing the amount of detected light decreases measurement uncertainty. Although the uncertainty in the parameters is rather high for each individual measurement within the time record, long data records allow for calculation of higher-accuracy statistical quantities such as power spectra and root-mean-square (rms) fluctuations.

III. Experimental Setup

The Rayleigh scattering diagnostic was applied in two heated jet facilities at GRC. The first demonstration was in a lab-scale electrically heated jet with a 10-mm-diam nozzle. The Rayleigh system was then installed in the SHJAR in GRC's Aeroacoustic Propulsion Laboratory. The SHJAR was equipped with a 50.8-mm-diam convergent nozzle, and the vitiated airflow was heated by a hydrogen combustor. The Rayleigh scattering system was used to measure temperature, axial velocity, and density fluctuations in both facilities. The goal of the testing in the SHJAR was to provide an experimental database, particularly of temperature fluctuation data, to be used for validation of computational codes.

A. Electrically Heated Nozzle Facility

Flow measurements were acquired in an electrically heated airflow issuing from a 10-mm-exit-diam convergent nozzle with a 200-mm-diam 10 m/s filtered-air coflow (Fig. 5). Because the measurement technique relied on having particulate-free gas flow, a series of filters were placed in line with the air plumbing to remove dust, oil, and water from the air supply before entering the nozzle flow system. The air issuing from the jet was heated by applying voltage to coils of wire inside the jet plenum. The coflow was provided by an air blower system equipped with submicron high-efficiency particulate air (HEPA) filters. Figure 5 shows the layout of the optics around the jet; these optics were used to collect Rayleigh scattered light from gas molecules in the flow. The jet was mounted such that the main flow direction was parallel to the table.

A Coherent Verdi 10 W, 532-nm-wavelength, single-frequency, Nd:Vanadate CW laser provided incident light for the system. The

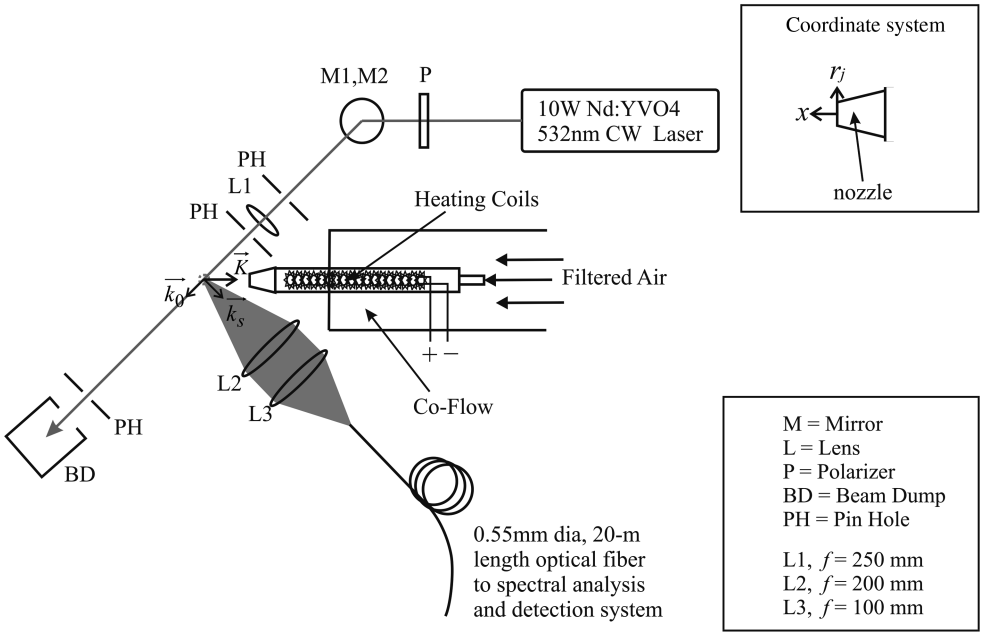

Fig. 5 Diagram of laser and collection optics for the electrically heated nozzle flow experiment.

laser had a line width of 5 MHz and frequency stability of approximately ±10 MHz. The laser line width was negligible in the calculation of temperature, because the Rayleigh spectral line width was on the order of 1 GHz. The vertically polarized laser beam was focused with a 250-mm-focal-length lens (L1) to a 70-μm $1/e^2$ diameter at the probe volume. The beam was oriented in the horizontal plane at a 45 deg angle to the primary flow direction. Light was collected at a 90 deg scattering angle, and two lenses imaged the collected light onto a 0.55-mm-diam multimode optical fiber.

Because the pair of lenses provided 1:2 imaging, the length of the probe volume in the laser-beam-propagation direction was 1.1 mm; however, the resolution in the radial direction, which was the direction of the velocity gradient of interest, was 0.78 mm. The 20-m-long optical fiber transmitted the scattered light to another area of the room in which the spectral analysis equipment was located. The incident and scattering wave vectors were arranged such that the axial component of the jet velocity u was measured, as indicated by the **K** vector in Fig. 5. As the laser beam propagated from the unheated ambient air through the heated jet air, the **K** vector changed slightly due to beam steering related to refractive index changes between the different-temperature airstreams. It was determined that laser beam deviation introduced less than 0.007% contribution of the radial component into the measured-velocity component, which was assumed to be negligible.

The jet was mounted on vertical and horizontal translation stages so that the probe volume could be positioned anywhere in the jet plume. The probe volume was positioned two jet diameters from the nozzle exit and was scanned radially at 1 mm increments across the flow, providing velocity, density, and temperature profiles at various flow conditions. The jet temperature was set by observing the output of a thermocouple in the jet plenum. A fixed power level was applied to the heater coils, which maintained a fixed air temperature for a fixed flow rate.

For calibration purposes, temperature, density, and velocity measurements were acquired in a steady laminar flow in the jet core. The total temperature was measured by a type K thermocouple with a 0.13 mm bead diameter. Two digital pressure gauges measured the ambient (static) pressure and the jet plenum (total) pressure. The velocity and density at the probe location within the core flow were calculated via isentropic flow and ideal-gas equations using total and static pressure and total temperature measurements. The calibration data were acquired in the core flow over a temperature range of 298 to 765 K and a velocity range of 14 to 110 m/s. The velocity and temperature fluctuations were verified using hot-wire anemometry and cold-wire thermometry systems.

The hot-wire and cold-wire systems could not be used at all flow conditions, due to physical limitations of the devices. Both of the fine wire probes were limited to a maximum temperature of 423 K. Also, the single-wire hot-wire system is not valid in flows with large temperature fluctuations, and the calibration must be performed at the flow temperature at which measurements are desired. Therefore, the hot-wire measurements were performed in unheated flows with mean velocities similar to the corresponding heated cases. Cold-wire data were only available at low-speed conditions, due to the fragility of the probe.

B. Small-Hot-Jet Acoustic Rig

The SHJAR is a vitiated-air-heated-jet facility that can cover the range of Mach numbers up to Mach 2 and static temperature ratios up to 2.8 using a hydrogen combustor and central air compressor facilities; however, the Rayleigh technique has only been applied to subsonic flows in this facility. The SHJAR is located in the AAPL at GRC. The AAPL is a 19.8-m-radius geodesic dome, with its interior covered by sound-absorbent wedges that provide the anechoic environment required to study propulsion noise from the SHJAR rig. The nozzle used in this test is one of a family of convergent nozzles, called the simple metal chevron (SMC) nozzles. For this test, the baseline nozzle SMC000 is used, which has a 50.8 mm exit diameter and a smooth round exit (no chevrons). A variety of conditions with acoustic Mach number Ma, which is defined as the jet exit velocity divided by the ambient sound speed (ranging from 0.5 to 1.59), and static temperature ratio TR (T_j/T_{amb}, ranging from 0.835 to 2.7), are covered in the test matrix; however, results from a single setpoint at $Ma = 0.5$ and TR = 1.765 are presented here. Measurements are acquired at several axial locations of $x/D \geq 2$ and radial locations of $0.0 \leq r_j/D \leq 1.25$.

A hydrogen combustor was used to avoid soot generation, because this molecular scattering technique required a clean gaseous flow. Burning hydrogen produced water vapor, which did not condense in the high-temperature plume. Flows with TR < 1 were also studied for calibration purposes, but condensation was not observed. The Rayleigh scattering cross section of water vapor is 13% lower than that of oxygen. Because the combustion process replaced some oxygen by water vapor, the Rayleigh scattering cross section for the heated air is expected to be different from the ambient. The difference, however, is calculated to be small (less than 0.5%). Other properties necessary for calculation of the Rayleigh spectrum that vary with temperature and gas composition included shear viscosity, thermal conductivity, molecular weight, internal specific heat, and

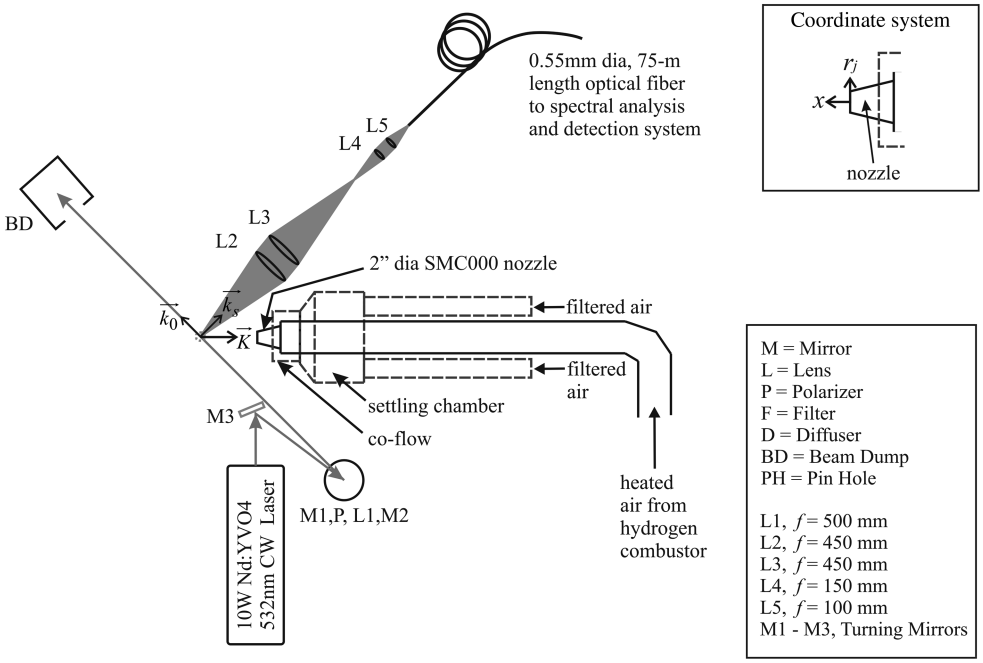

Fig. 6 Diagram of laser and collection optics in the SHJAR facility.

bulk viscosity. The values for each of these properties are expected to vary by less than 2% between the moist heated air and the ambient air. These calculations were based on a global equivalence ratio of approximately 0.1, with hydrogen and air mass flow rates of 0.00069 kg/s and 0.23 kg/s, respectively. No special steps were taken to account for the differences that have manifested as sources of measurement uncertainty.

The laser and collection optics portion of the Rayleigh scattering system are shown around the SHJAR in Fig. 6. A coflow system was built specifically for this test (components are shown in dashed lines in Fig. 6) to provide a low-speed particulate-free airstream around the jet core. Room air was filtered by a blower system equipped with submicron HEPA filters and was routed to the settling chamber via two 200 mm flex-duct sections and exhausted around the nozzle through a straight 250-m-long section of 305-mm-diam pipe. A screen was positioned between the settling chamber and the straight exhausting duct section to break up turbulence and straighten the flow.

The top view of the facility shown in Fig. 6 illustrates the laser beam propagation and scattered-light collection. The laser head of a laser system identical to that used in the first experiment was located about 1 m below the scattering plane, and an enclosed box containing two turning mirrors, a polarizer, and the focusing lens routed the beam upward (out of the plane of the page in Fig. 6) and through the centerline of the jet flow. The vertically polarized laser beam was focused with a 500-mm-focal-length lens (L1) to a 140-μm $1/e^2$ diameter at the probe volume. The beam was oriented in the horizontal plane at a 45 deg angle to the primary flow direction. Light was collected at a 90 deg scattering angle, collimated, and focused by a pair of f3 450-mm-focal-length lenses (L2 and L3), then reimaged by another pair of lenses with focal lengths of 150 and 100 mm (L4 and L5, respectively) onto a 0.55-mm-diam multimode optical fiber. Because the train of lenses provided 1:1.5 imaging, the length of the probe volume in the laser-beam-propagation direction was 0.825 mm, providing resolution in the radial direction of 0.58 mm.

The incident and scattering wave vectors were arranged such that the axial component of the jet velocity u was measured, as indicated by the **K** vector in Fig. 6. As in the previous experiment, beam steering due to refractive index changes between the hot and cold airstreams was determined to have a negligible effect on the measured-velocity component. The laser, beam-propagation optics, and collection optics were all mounted on a large x–y traversing system (not shown in the figure) so that the probe volume could be positioned at various locations in the jet flow. The 75-m-long optical fiber transmitted the scattered light to an adjacent building in which the sensitive spectral analysis equipment was located.

For calibration purposes, temperature, density, and velocity measurements were acquired in a steady laminar flow in the jet core. Calibration data were acquired in the core flow over a jet exit temperature range of 239 to 630 K and a velocity range of 167 to 300 m/s. The flow was subsonic for all calibration points; therefore, the velocity, static temperature, and density were calculated assuming isentropic expansion of an ideal gas. The lowering of specific heat ratio with increasing temperature was taken into account in these calculations by using the assumption of a simple harmonic vibrator to account for the contribution of the vibrational heat capacity to the specific heats, following Eq. 180 of [30] for a thermally perfect gas.

Following the calibration, data were acquired at various radial and axial locations for jet exit conditions of 500 K and 167 m/s. The optical system losses in this facility reduced the signal strength by about one-half compared with the signals observed in the electrically heated jet experiment. The reduction in f-number provided a larger collection solid angle in the SHJAR facility, which should have accounted for the reduction of signal, due to a shorter probe volume length and longer optical fiber. The lower signal strength compared with the electrically heated jet system indicates that the transmission efficiency of the fiber may have been reduced by damage or extreme bending somewhere along the length of the fiber. Therefore, the data were sampled at a rate of 10 kHz for this test to achieve signal levels similar to the electrically heated experiment. Previous velocity data acquired using TR-PIV [11] at 10 kHz data rate are shown for comparison.

C. Spectral Analysis and Detection Optics

The spectral analysis and detection optics were identical for both experiments. Upon collection of the Rayleigh scattered light by the 0.55-mm-diam multimode fiber, it was routed to a separate area, shown schematically in Fig. 7. The light exiting the fiber was collimated by an 80-mm-focal-length f1.6 lens (L6) and was directed through the planar-mirror Fabry–Perot interferometer. The FPI had 70-mm-diam mirrors with 80% reflectivity, 8.7 GHz free spectral range, and reflective finesse of approximately 15. The Fabry–Perot is an extremely sensitive instrument: even the smallest vibrations or temperature changes can cause the mirrors to drift out of

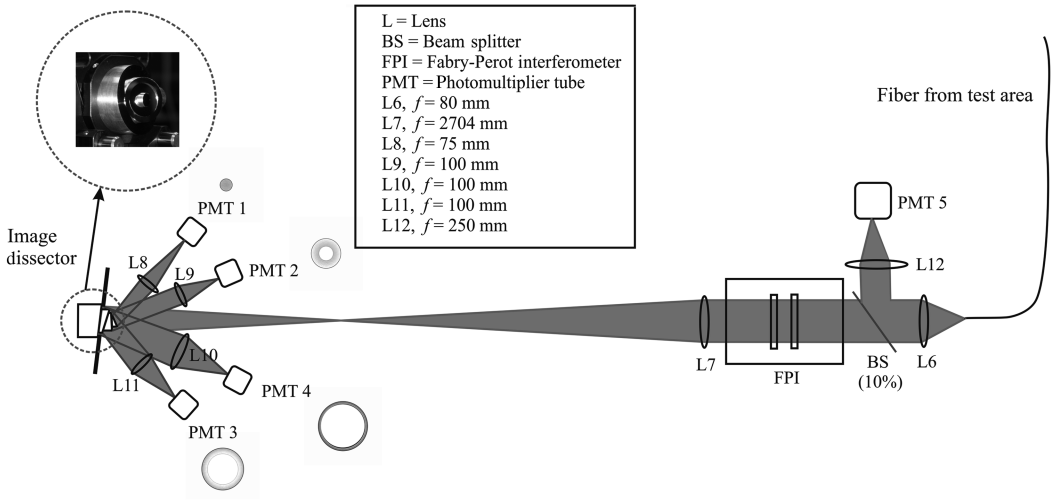

Fig. 7 Schematic of spectral analysis and detection optics.

parallel alignment, resulting in increased uncertainty. Therefore, a stabilization system [28] was used to maintain parallelism of the mirrors and to set the fringe diameter of the incident reference light to 13 mm for the electrically heated jet experiment and to 14.4 mm for the SHJAR test.

The Rayleigh scattered light exiting the FPI was focused by a fringe-forming lens (L7) with an effective focal length of approximately 2700 mm, which provided a 18.6-mm-diam image of the fiber face. Light from circular and annular sections of the image was directed toward PMTs by a concentric elliptical mirror system, which was designed and fabricated specifically for this application. A photograph of the image dissector is shown in the upper left corner of Fig. 7. The mirrors have 12 deg elliptical surfaces with about 90% reflectivity. The mirror diameters, from innermost to outermost, were 5, 12, 16, and 25 mm. Each mirror sent the respective portion of the fringe image toward PMTs 1, 2, 3, and 4, as shown in Fig. 4; the fringe regions are also illustrated near the corresponding PMT in Fig. 7.

The PMTs consisted of Hamamatsu model R9110 detector tubes with approximately 20% quantum efficiency (QE) at a 532 nm wavelength, which were mounted in model PR1405SHCE housings by Products for Research. The PMTs were operated in the photon-counting mode to acquire fringe-intensity data. Each PMT was supplied with 1200 V, and the varying-amplitude photoelectron pulses from the five PMTs were amplified with a gain of 5 and were counted by Stanford Research model SR400 photon counters, which output negative-amplitude pulses for each incoming photoelectron pulse with an amplitude exceeding the threshold level. Typical threshold levels ranged from −25 to −50 mV for the five PMTs. Canberra model 2126 constant fraction discriminators converted the negative-amplitude pulses to positive-amplitude 2.5 V pulses that were counted by two National Instruments model 6602 counter-timer boards. Typical photoelectron count rates for this work were on the order of 1 MHz.

A PC-based data acquisition system using National Instruments data acquisition hardware and LabVIEW software was used to record the signals from the PMTs. Each signal channel was digitized for 5.12 s at a 32 kHz sampling rate in the first experiment and for 7.98 s at a 10 kHz sampling rate in the second experiment. The intensity information from the Fabry–Perot fringe sampling was used to obtain temperature and velocity measurements. The density measurement was much simpler, requiring only an overall intensity measurement. A beam splitter located just in front of the FPI input (Fig. 7) directed approximately 10% of the incoming Rayleigh scattered light to a lens (L12) that focused the light at PMT 5 for the density measurement. The photoelectron counts recorded by PMT 5 were linearly related to density, which provided an independent yet simultaneous measurement of density, along with the velocity and temperature measurements from spectroscopic analysis.

IV. Data Analysis

A. Experiment Calibration and Data Analysis Method

For calibration, the electrically heated jet was operated over a temperature range of 298–765 K and velocity range of 14–110 m/s, and the SHJAR was operated over a temperature range of 239–630 K and velocity range of 167–300 m/s. At these operating points, mean temperature, velocity, density, and pressure were calculated assuming isentropic expansion of an ideal gas. The linear relationship between photon counts measured by PMT 5 and theoretical gas density was established. Figure 8 shows the density calibration curves for the two experiments, along with the linear curve fit for each set of data.

Several unknown parameters, such as system-detection efficiencies, effective finesse of the FPI, and fringe-forming-lens focal length, were evaluated by MLE analysis of the mean photon-count data using the theoretical calculated flow properties as known values for temperature, velocity, density, and pressure in the model function. The overall efficiency ε, including collection losses, transmission losses through the optical fiber, and QE of the detectors, was found to be approximately 2% for the electrically heated jet experiment and 1% for the SHJAR experiment. Adjustment of the exact efficiency values was necessary for each PMT in the system due to minor differences in each detector's QE. The finesse and fringe-forming-lens focal length were found to be approximately 15 and 2.7 m, respectively. Once determined, these parameters were input into the model function for use in MLE analysis of the PMT counts for temperature and velocity measurements. Figures 9 and 10 show the mean velocity and temperature measured by the Rayleigh

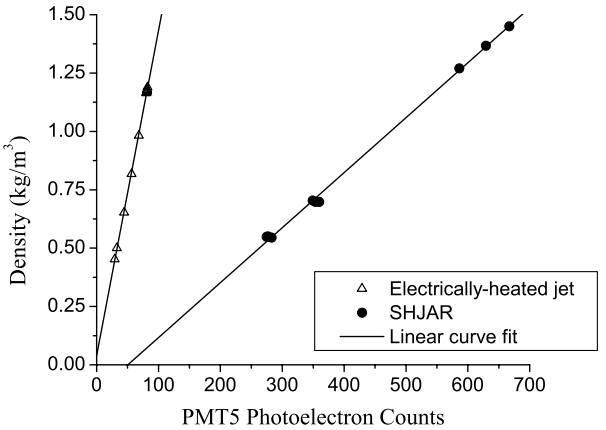

Fig. 8 Density calibration curves showing the relationship between photoelectron counts and gas density for both experiments.

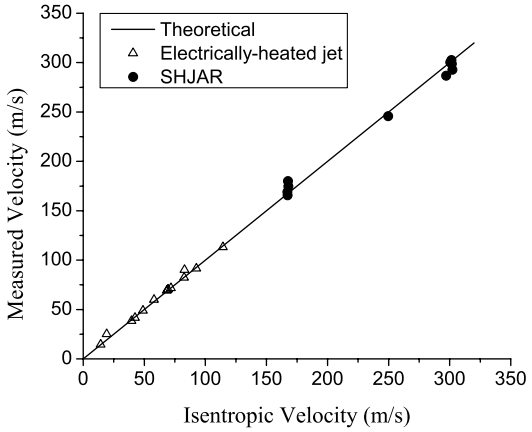

Fig. 9 Velocity measured by Rayleigh technique compared with theoretical isentropic velocity for both experiments.

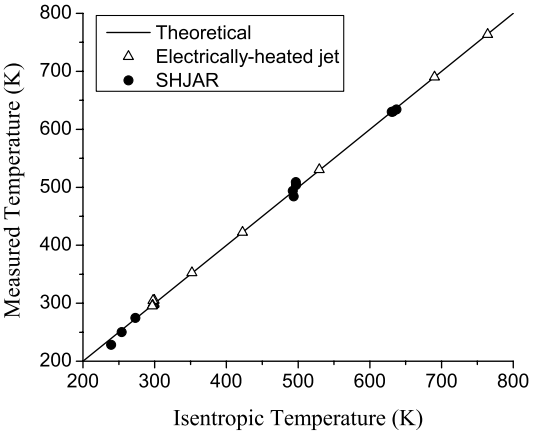

Fig. 10 Temperature measured by Rayleigh technique compared with theoretical isentropic temperature for both experiments.

technique compared with the theoretically predicted values for the calibration flow conditions in both experiments. The mean values were within 7 m/s and 7 K of the theoretical values for velocity and temperature, respectively.

Using the linear relation between PMT 5 photon counts and density and MLE analysis of the photon counts from PMTs 1–4, time histories of density, temperature, and velocity were evaluated. Although a constant static pressure equivalent to the ambient pressure was probably a valid assumption in these subsonic free-jet experiments, the pressure was assumed to be unknown. The density measured by PMT 5 and the temperature estimate from MLE analysis of PMTs 1–4 photon counts were used to determine the local pressure using the ideal-gas law to demonstrate that this technique was applicable in flows in which the pressure was unknown and the ideal-gas law was valid.

B. Power Spectral Calculations

The mean velocity, temperature, and density were calculated and subtracted from their respective time-history records to provide zero-mean records, which were used to calculate the power spectral densities of the property fluctuations. Because of the shot noise in the PMT signals, it was necessary to use relatively long data records and calculate power spectra using a technique known as the Welch method of modified periodograms [31]. In the Welch method, a data record sampled at a rate $f_s = 32$ kHz (10 kHz) was subdivided into smaller records of length $L = 4096$ (1024) samples, which were overlapped by 50%. The modified periodograms of each subrecord were calculated using a Welch data window. These individual periodograms were then averaged to obtain the estimate of the power spectrum and divided by the frequency resolution (f_s/L) to obtain the power spectral density (PSD). The number of individual periodograms used to calculate the averaged PSD depended on the length of the record used. The 5.12 s data records resulted in 78 overlapped segments, and the 7.98 s data records resulted in 154 overlapped segments. Overlapping the segments by 50% provided a near-maximum reduction in the variance in the spectral estimate [31]. The resulting PSDs provided fluctuation information up to half of the sampling frequency, and the integral of the PSD was equivalent to the mean square fluctuations. The PSDs were smoothed using a five-point moving-average filter.

Two numerical processing methods exist that are commonly used to eliminate noise from power-spectral-density estimates. The first involves simply subtracting the noise floor from the spectra. Shot noise is broadband noise that contributes equally over all frequencies; therefore, it causes a constant offset in the spectrum. If the spectrum flattens out at high frequencies due to the lack of significant fluctuations, then the average value of this noise floor can be estimated and subtracted from every point in the spectrum, thereby eliminating the broadband shot-noise contribution. The second method, which is only possible if you have two simultaneous measurements of the same property, is to take the cross spectrum of the two simultaneous measurements [32]. Any uncorrelated noise is eliminated from the final spectrum. One way to obtain two simultaneous measurements is to split the light into two separate paths and individually analyze each beam path. This would require a secondary set of all spectral analysis and detection equipment, which is not very practical. Therefore, the noise-floor subtraction method was chosen to eliminate measurement shot noise in the data presented in this paper; the noise floor was estimated from the last 500 Hz of the power spectrum.

V. Results and Discussion

A. Data from the Electrically Heated Jet Experiment

The electrically heated jet was operated at conditions that provided moderate temperature and velocity levels at which resistance probes were applicable for measurement comparisons. The Rayleigh probe volume and the hot-wire and cold-wire probes were scanned horizontally across the centerline of the electrically heated jet at an axial station of $x/D = 2$. Scans of the Rayleigh probe volume were performed at jet-exit conditions of 420 K and 110 m/s (case 1) and 420 K and 38 m/s (case 2). Because of the fragility of the cold-wire probe, it could be used to provide mean and rms temperature measurements in the low-velocity flow only. The hot-wire probe also had physical limitations, leading to the inability to make measurements in heated flows. Therefore, hot-wire measurements were performed in cold flows with maximum velocities similar to the heated-flow cases. The radial scans provided measurements in the jet core as well as in the turbulent mixing layer formed between hot and cold airstreams. The mean temperature T and velocity u values for the Rayleigh measurements were calculated from the time-history data, and the rms temperature T' and velocity u' fluctuations were calculated from the integral of the PSD after the noise floor had been subtracted.

Figure 11 shows a radial profile of normalized mean velocity at $x/D = 2$, and Fig. 12 shows a radial profile of rms velocity fluctuations normalized by the jet-exit velocity U_j. The error bars in Fig. 11 represent the rms error due to shot noise σ_{u_k}, which was calculated using the CRLB analysis discussed in Sec. II.B. The rms error is greater in the hot-jet core than in the ambient air, due to a lower signal-to-noise ratio as a result of a reduction in molecular number density. The error bars for the rms velocity-fluctuation measurements in Fig. 12 were determined based on the noise floor and variance of the PSDs that were used to calculate the u' estimates. Error in u' due to the shot-noise floor was estimated from the CRLB analysis, whereas the rms error in u' due to PSD variance was calculated from the rms fluctuations in the actual PSD estimate over the last 500 Hz ($\sigma_{u-\mathrm{PSD}}$). These error sources are combined in the following expression, in which the first term is associated with the noise floor and the second term is associated with the PSD variance:

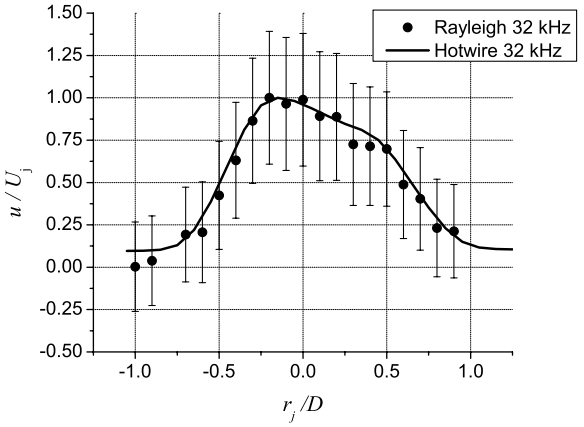

Fig. 11 Normalized mean velocity profile calculated from Rayleigh data in a flow with jet exit temperature and velocity of $T_j = 420$ K and $U_j = 110$ m/s, and hot-wire measurements in a room-temperature flow with similar maximum velocity.

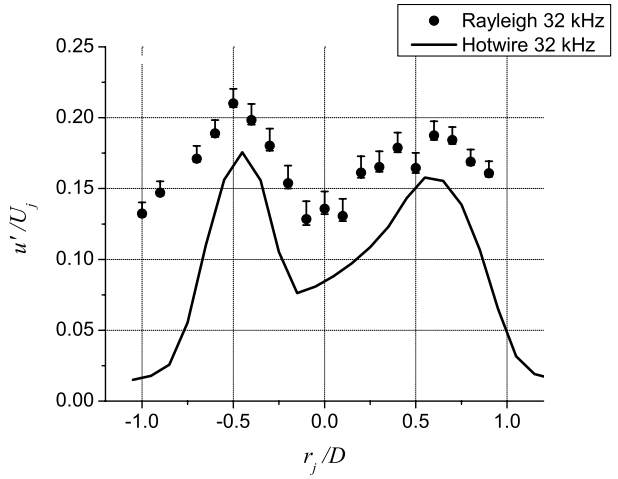

Fig. 12 Normalized rms velocity-fluctuation profile calculated from Rayleigh measurements in a flow with jet exit temperature and velocity of $T_j = 420$ K and $U_j = 110$ m/s and hot-wire measurements in a room-temperature flow with similar maximum velocity.

$$u'_{\text{error}} = -\frac{\sigma_{u_k}}{\sqrt{L/2}} \pm \sqrt{\frac{f_s}{L}\sigma_{u-\text{PSD}}} \tag{12}$$

The error associated with the noise floor, which is the largest error source, results in a potentially lower estimate of u' than the actual value; therefore, the error associated with the noise floor is only in the positive direction in Fig. 12. The noise-floor error source is significantly greater than the error due to PSD variance, as evidenced by the much larger error in the positive direction in Fig. 12.

The Rayleigh measurements presented in Figs. 11 and 12 are compared with hot-wire velocity measurements acquired in an unheated flow at the same maximum velocity as the heated flow of case 1. The asymmetry of the velocity profiles is caused by flow disturbance from the heater coils in the jet plenum. The mean velocities from the Rayleigh measurements show some deviation from the hot-wire measurements at a few points in the radial profile. The Rayleigh velocity measurements in the low-velocity region of the coflow tend to be biased toward lower values than those measured by the hot-wire probe by as much as 5–10 m/s. The agreement between the measurements gets better as velocity increases; the Rayleigh measurements agree with the hot-wire measurements within 5 m/s throughout most of the profile. The laser used for these measurements is not frequency-stabilized; there is inherent drift in the laser frequency over time.

Previous analysis [28] quantified the amount of velocity error induced by frequency drift of this particular laser system. The expected laser frequency drift on the order of 10 MHz over the time period of the Rayleigh data acquisition leads to potential velocity bias error on the order of 4 m/s. Error due to the accuracy with which the reference fringe radius is set by the Fabry–Perot stabilization system results in additional bias error of up to 2 m/s. The hot-wire measurements provide shear-layer fluctuation levels of $0.15U_j$ to $0.18U_j$, which corresponds to typical shear-layer fluctuations measured in heated jets by TR-PIV [11]; however, the Rayleigh measurements indicate fluctuation levels that are greater than the hot-wire data by $0.02U_j$ to $0.035U_j$ at the peaks and as much as $0.12U_j$ in other regions of the profile. The discrepancies may be due to erroneous velocity fluctuations related to instability of the Rayleigh laser frequency or limitations due to the Poisson noise that is inherent in this technique.

Figure 13 shows the radial profile across the jet flow at $x/D = 2$ of normalized mean temperature, and Fig. 14 shows the radial profile of rms temperature fluctuations normalized by the difference between the jet exit temperature and the ambient temperature ($T_j - T_{\text{amb}}$). The error bars indicated in both figures were determined using the same approach as previously described for the mean and rms velocity measurements. The rms error in the mean temperature is based on the error due to shot noise (σ_T) evaluated by the CRLB analysis. The error in rms temperature was evaluated from the noise floor and

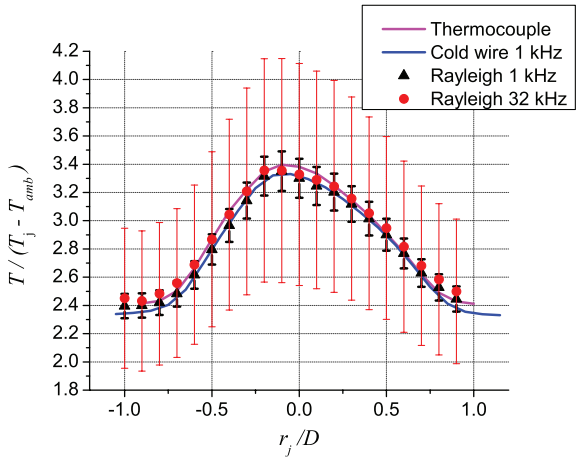

Fig. 13 Normalized mean temperature profile calculated from Rayleigh and cold-wire data and measured by a thermocouple for a flow with jet exit temperature and velocity of $T_j = 420$ K and $U_j = 38$ m/s.

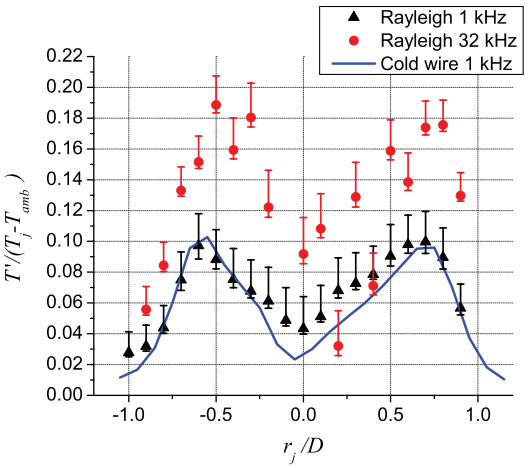

Fig. 14 Normalized rms temperature fluctuation profile calculated from Rayleigh and cold-wire measurements in a flow with jet exit temperature and velocity of $T_j = 420$ K and $U_j = 38$ m/s.

variance of the PSDs that were used to calculate T' using the following expression:

$$T'_{\text{error}} = -\frac{\sigma_T}{\sqrt{L/2}} \pm \sqrt{\frac{f_s}{L}\sigma_{T-\text{PSD}}} \tag{13}$$

The error due to the noise floor, which is represented by the first term in Eq. (13), makes the greatest contribution to the error in T'.

The 1 and 32 kHz rate Rayleigh measurements are compared with thermocouple and 1 kHz cold-wire temperature measurements in Figs. 13 and 14. The mean temperatures from the Rayleigh technique compare well with the thermocouple measurements that were acquired in the flow just before the Rayleigh data acquisition and with the cold-wire measurements that were acquired on a different day, with the greatest deviation being less than 2%. The 1 kHz Rayleigh rms temperature fluctuations match the 1 kHz cold-wire measurements very well in Fig. 14. The largest deviation between the two measurements is approximately 0.015 $(T_j - T_{\text{amb}})$ and occurs in the jet core. A much greater deviation occurs between the 1 and 32 kHz data; the reason for this is explained as follows.

Figure 15 shows the temperature PSD at $r_j/D = 0.7$ calculated from 1 and 32 kHz rate Rayleigh and 1 kHz rate cold-wire measurements; the 1 kHz spectra are calculated using 128 point segments so that the periodograms match the frequency resolution of the 32 kHz spectrum. The cold-wire measurements provide accurate turbulence levels for fluctuations up to 500 Hz, but significant temperature fluctuations exist at higher frequencies, as shown in Fig. 15. If the data are significantly undersampled in frequency and anti-alias filtering is not employed, aliasing of the higher-frequency content in the flow beyond the sampling rate should manifest itself across the entire frequency range of the spectrum, often resulting in a rise in the tail of the spectrum [11]. There may be some evidence of aliasing in the 1 kHz spectra in Fig. 15. Because the 1 kHz cold-wire and Rayleigh measurements do not properly account for higher-frequency fluctuations, the resulting turbulence levels from the 1 kHz data sets result in lower fluctuation estimates than the 32 kHz data, hence the discrepancy in the rms temperature fluctuations in Fig. 14.

Both 1 and 32 kHz Rayleigh temperature PSDs compare quite well with the cold-wire PSD in the frequency range from 0 to 500 Hz, which indicates that the Rayleigh technique provides good estimates of the temperature fluctuations. The peak temperature fluctuations calculated from the 32 kHz Rayleigh temperature measurements range from 16 to 19% of $T_j - T_{\text{amb}}$. Khavaran and Kenzakowski [33] provide CFD predictions of total temperature fluctuations using a Reynolds-averaged Navier–Stokes (RANS) solver. Although the static and total temperature fluctuations are expected to vary slightly, a comparison between the CFD prediction should indicate if the Rayleigh measurements are at least in the right range. The numerical calculations indicate that the total temperature fluctuations in the shear layer for heated round jets in this temperature range should be on the order of 15% relative to the difference between the jet exit temperature and the ambient. Therefore, the Rayleigh measurements in the shear layer appear to be slightly high. Greater error is expected in the lower-amplitude fluctuation measurements, in which the fluctuation level falls within the noise level of the technique.

B. Data from the SHJAR

The SHJAR was operated at jet exit conditions of $U_j = 167$ m/s and $T_j = 500$ K ($Ma = 0.5$ and TR = 1.765), and the Rayleigh probe volume was scanned horizontally from the jet centerline ($r_j/D = 0$) outward through the shear layer at axial locations of $x/D = 2$, 3, 5, and 6. The flow is symmetric about the axis for this round-nozzle flow. TR-PIV data were acquired at 10 kHz rate in the same facility before this test [11] and are included here for comparison with the Rayleigh measurements. Both the nozzle flow and ambient air were seeded in that work to achieve velocity measurements in the core as well as the mixing layer. The hot nozzle flow was seeded with 0.5-μm-diam alumina powder, whereas the ambient fluid was seeded with 0.3 μm mineral-oil droplets produced by a commercial smoke generator.

Figure 16 shows mean velocity normalized by the jet exit velocity as a function of normalized radial position (r_j/D) for Rayleigh and TR-PIV data acquired at a sampling rate of 10 kHz. Only one-half of the jet profile was measured by the Rayleigh technique, because the flow is symmetric about the axis in this case. The rms error in velocity due to shot noise ranged from ± 0.14 to ± 0.27 relative to U_j; error bars have been omitted from Fig. 16 to avoid unnecessary clutter due to the large error bars. Some differences in the mean velocities exist between the two measurements. The centerline velocities are in agreement; however, the Rayleigh data offcenterline show an underestimation of the mean velocities compared with the TR-PIV measurements. It is not clear whether this difference physically exists or if it is related to bias error in the Rayleigh measurements; however, the general trend in profile development as the flow progresses downstream follows that predicted by the TR-PIV data.

Figure 17 shows radial profiles of rms velocity fluctuations normalized by the jet exit velocity based on the two measurement techniques. The error bars shown for the Rayleigh turbulence fluctuation estimates were calculated using Eq. (12). Again, there are differences between the Rayleigh and TR-PIV measurements, which may be explained by observation and discussion of the PSDs that were used to determine the rms values.

Velocity PSDs calculated from Rayleigh and TR-PIV data acquired at $r_j/D = -0.5$ and $x/D = 2$, 3, 5, and 6 are shown in Figs. 18–21, respectively. The broadband noise floor has been subtracted from all Rayleigh PSDs, and the rms fluctuations displayed in Fig. 17 were evaluated from the integral of the PSDs. Obtaining accurate PSD and rms fluctuation estimates relies on two assumptions:

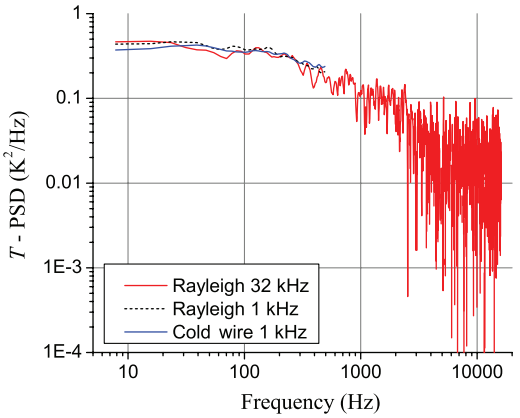

Fig. 15 Temperature PSD calculated from Rayleigh and cold-wire measurements in a flow with jet exit temperature and velocity of $T_j = 420$ K and $U_j = 38$ m/s.

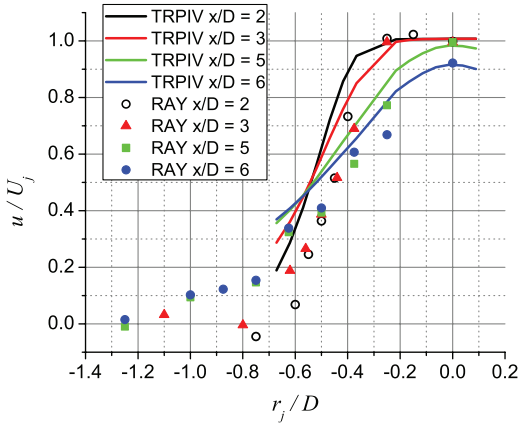

Fig. 16 Normalized mean velocity as a function of r_j/D at jet exit conditions of $T_j = 500$ K and $U_j = 167$ m/s in the SHJAR facility; 10 kHz Rayleigh measurements are compared with 10 kHz TR-PIV data.

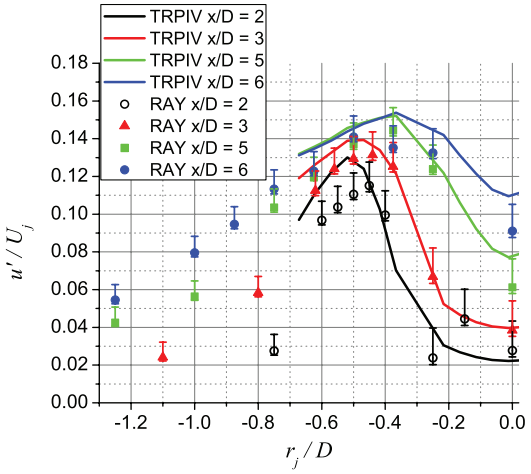

Fig. 17 Normalized rms velocity fluctuations as a function of r_j/D at jet exit conditions of $T_j = 500$ K and $U_j = 167$ m/s in the SHJAR facility. 10 kHz Rayleigh measurements are compared with 10 kHz TR-PIV data.

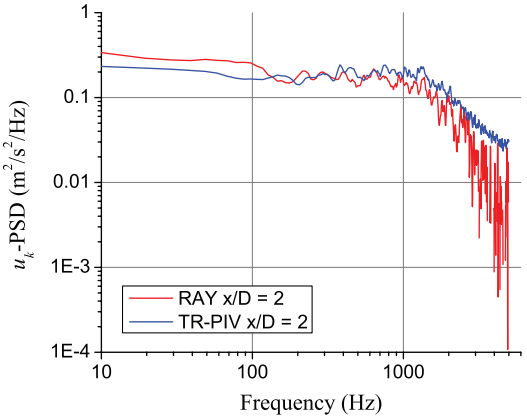

Fig. 18 Velocity PSD calculated from 10 kHz Rayleigh and TR-PIV data acquired at $x/D = 2$ and $r_j/D = -0.5$ in the SHJAR with jet exit conditions of $T_j = 500$ K and $U_j = 167$ m/s.

1) The noise floor is sufficiently represented by the average spectral value over the last 500 Hz.

2) Any energy in the spectrum that falls below the noise-floor level does not make a significant contribution to the rms fluctuations.

If these two assumptions are not met, the noise-floor subtraction technique may cancel out energy that is not purely noise. This tends to be a problem in regions in which higher-frequency fluctuations are

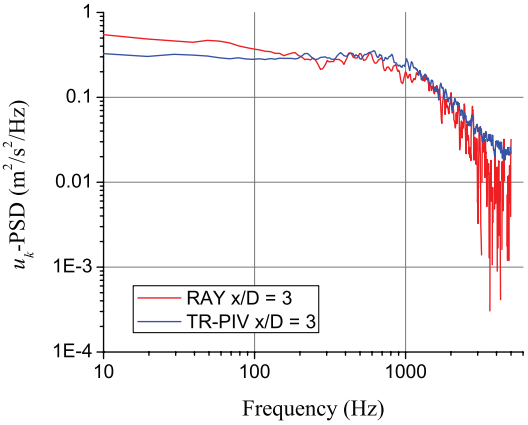

Fig. 19 Velocity PSD calculated from 10 kHz Rayleigh and TR-PIV data acquired at $x/D = 3$ and $r_j/D = -0.5$ in the SHJAR with jet exit conditions of $T_j = 500$ K and $U_j = 167$ m/s.

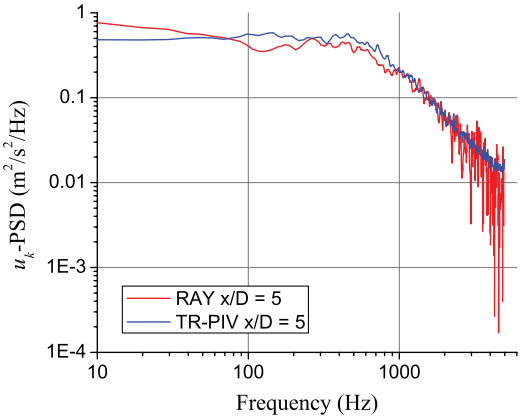

Fig. 20 Velocity PSD calculated from 10 kHz Rayleigh and TR-PIV data acquired at $x/D = 5$ and $r_j/D = -0.5$ in the SHJAR with jet exit conditions of $T_j = 500$ K and $U_j = 167$ m/s.

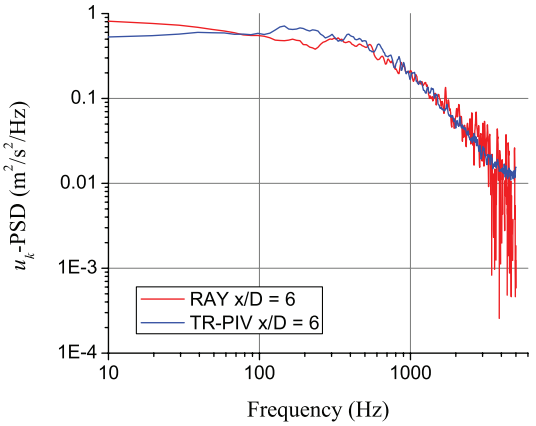

Fig. 21 Velocity PSD calculated from 10 kHz Rayleigh and TR-PIV data acquired at $x/D = 6$ and $r_j/D = -0.5$ in the SHJAR with jet exit conditions of $T_j = 500$ K and $U_j = 167$ m/s.

expected, because the spectrum is less likely to have reached the noise-floor level by the last 500 Hz of the frequency range.

Higher-frequency content is usually expected as you approach the nozzle exit plane. The Rayleigh velocity PSDs for $x/D = 2$ and 3 (Figs. 18 and 19) have lower energy levels over frequencies greater than 200 Hz, compared with the TR-PIV PSDs. This results from an overestimation of the noise floor. Further downstream [$x/D = 5$ and 6 (Figs. 20 and 21)], the Rayleigh and TR-PIV PSDs match up better because the noise floor was more accurately represented by the energy level at 4.5 kHz and beyond. Therefore, it is important to consider the expected fluctuation range when implementing the Rayleigh technique, because under-resolving the frequencies can result in an artificially high noise-floor estimate and hence a low rms fluctuation estimate for the measured flow properties. The turbulence spectra within the first diameter of the nozzle exit are dominated by high frequencies on the order of 100 kHz, whereas the frequencies further downstream typically do not exceed 30–40 kHz [11].

As previously mentioned, if the data are significantly undersampled in frequency, aliasing of the higher-frequency content often results in a rise in the tail of the spectrum. It is not possible to antialias filter the Rayleigh or TR-PIV data when they are acquired, which is the standard approach in other techniques such as hot-wire anemometry. The effects of aliasing on the power spectral densities for undersampled data have been investigated by Wernet [11]; these effects may be evident in under-resolved situations such as the 10 kHz data acquired in the SHJAR facility close to the nozzle, in which fluctuations up to 40 kHz are expected (Figs. 18 and 19).

Figures 22 and 23 show radial profiles of mean and rms temperature, respectively, measured by the Rayleigh technique normalized by the difference between the jet exit and ambient

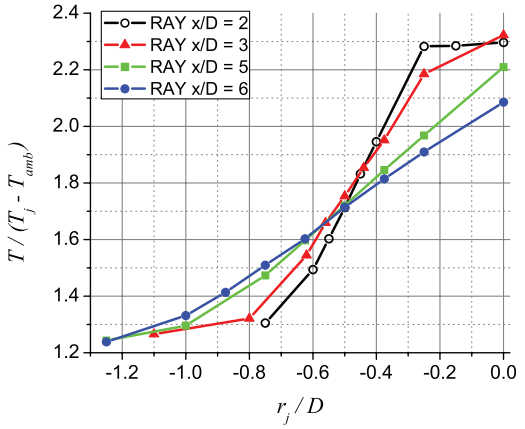

Fig. 22 Normalized mean temperature as a function of r_j/D at jet exit conditions of $T_j = 500$ K and $U_j = 167$ m/s in the SHJAR facility calculated from 10 kHz Rayleigh data.

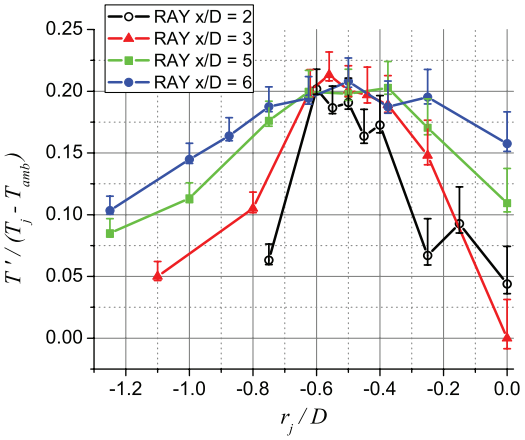

Fig. 23 Normalized rms temperature fluctuations as a function of r_j/D at jet exit conditions of $T_j = 500$ K and $U_j = 167$ m/s in the SHJAR facility calculated from 10 kHz Rayleigh data.

temperatures ($T_j - T_{\text{amb}}$) for the same jet conditions of $T_j = 500$ K and $U_j = 167$ m/s. Although error bars have been omitted from Fig. 22, it should be noted that the rms error in the mean temperature based on the error due to shot noise ranged from ± 0.2 to ± 0.5 of the difference between jet exit and ambient temperatures. The error bars for the error in the rms temperature measurements were evaluated using Eq. (13) and are indicated in Fig. 23.

Dynamic temperature data by another experimental technique are not available for comparison; however, shear-layer total temperature rms fluctuations based on RANS CFD predictions for a round-nozzle flow with the same conditions were presented by Khavaran and Kenzakowski [33]. Their calculations indicate that total temperature fluctuations in the shear layer should be on the order of 16% relative to the difference between jet exit and ambient temperatures. The shear-layer static temperature fluctuations measured by the Rayleigh technique are slightly higher than the predicted total temperature fluctuations, with levels of 20-22% of $T_j - T_{\text{amb}}$.

Khavaran and Kenzakowski [34] also presented the static and total temperature fluctuations along the centerline of the jet based on RANS CFD predictions. The CFD predictions estimated temperature fluctuations on the centerline for $x/D \leq 3$ as 0.3% of $T_j - T_{\text{amb}}$. The Rayleigh centerline measurement of T' at $x/D = 2$ and 3 are not expected to be accurate, because the amplitude of the fluctuations falls within the noise level of the technique. The CFD-predicted temperature fluctuation levels at $x/D = 5$ and 6 are approximately 3.5 and 10% of $T_j - T_{\text{amb}}$, respectively. The corresponding Rayleigh centerline measurements of T' are about 11 and 16% of $T_j - T_{\text{amb}}$ for $x/D = 5$ and 6, respectively. Temperature fluctuation levels that are greater than 2.5% of $T_j - T_{\text{amb}}$ are expected to be above the noise-floor level; therefore, the high estimates of T' compared with the CFD predictions need to be investigated further. The shear-layer growth and mean temperature profile development appear to follow the same trends as the RANS CFD predictions [33,34].

VI. Conclusions

A technique for obtaining gas velocity, temperature, and density measurements at high sampling rates using molecular Rayleigh scattering was described. Density was determined from an overall intensity measurement of the scattered light, whereas temperature and velocity were determined by analyzing the scattered light with a Fabry–Perot interferometer. The signals from five photomultiplier tubes were simultaneously recorded using photon-counting at sampling rates up to 32 kHz. Uncertainties in individual temperature and velocity measurements within the time record are estimated to be on the order of 20% and 30 m/s, respectively. Other statistical quantities, such as root-mean-square fluctuations and power spectra, can be obtained with higher accuracy by using the Welch method of modified periodograms and noise-floor subtraction. The Rayleigh technique was demonstrated in two hot-jet facilities: an electrically heated jet with a 10-mm-diam nozzle and the small-hot-jet acoustic rig (SHJAR) with a 50.8-mm-diam nozzle in GRC's Aeroacoustic Propulsion Laboratory. Rayleigh measurements were validated by comparison with hot-wire anemometry, cold-wire thermometry, and TR-PIV measurements. The complete set of data acquired in the SHJAR will be analyzed and presented in a later publication to provide an experimental database for validation of computational codes.

This Rayleigh technique has proven useful in studying subsonic heated jets. The technique has a limited velocity and temperature range; the exact range of usefulness varies depending on the experimental arrangement and equipment. Based on the free spectral range of the FPI and imaging parameters of the lenses used in this work, velocities up to 650 m/s can theoretically be measured. However, the usefulness of the technique in that velocity range is questionable, as shocks may cause extreme changes in the beam-propagation direction that could prohibit collection of the scattered light or significantly change the direction of the measured-velocity component. Further investigation is planned to assess the usefulness of this technique in the presence of shocks. The maximum temperature that can be measured is limited by the signal-to-noise ratio achievable by the system, because the scattering signal decreases as temperature increases. Also, particulates in the gas flow are problematic for this technique; therefore, it is important to use a very clean gas supply and to avoid condensation of vapors in the flow. It is important to keep in mind the expected frequencies of the property fluctuations in an experiment and to attempt to use a minimum data rate not less than twice the maximum expected frequency, if possible, to avoid aliasing and noise-floor estimation errors. The maximum sampling rate, however, is also limited by the signal-to-noise ratio, because a higher sampling rate results in a shorter integration time over which signal photons are detected.

Acknowledgments

The authors would like to thank Dennis Eck of Jacobs Sverdrup and Ray Loew of Sierra Lobo for their support in the setup and operation of the small-hot-jet acoustic rig facility and Pete Eichele of Gilcrest for his assistance in the setup and installation of the Rayleigh scattering system. We would also like to thank Mark Wernet of the Optical Instrumentation and Nondestructive Evaluation Branch and James Bridges of the Acoustics Branch at NASA John H. Glenn Research Center at Lewis Field for providing the temporally resolved particle image velocimetry data that were presented and Giuseppe Tenti of the University of Waterloo for providing the 6-moment Rayleigh spectrum calculation code.

References

[1] Eckbreth, A. C., *Laser Diagnostics for Combustion Temperature and Species*, Gordon and Breach, Amsterdam, 1996, pp. 209–451.

[2] Cummings, E. B., "Laser-Induced Thermal Acoustics," Ph.D. Dissertation, Dept. of Engineering and Applied Science, California Inst. of Technology, Pasadena, CA, 1995.
[3] Hart, R. C., Balla, R. J., and Herring, G. C., "Nonresonant Referenced Laser-Induced Acoustics Thermometry in Air," *Applied Optics*, Vol. 38, No. 3, 1999, pp. 577–584. doi:10.1364/AO.38.000577
[4] Boguszko, M., and Elliott, G. S., "On the Use of Filtered Rayleigh Scattering for Measurements in Compressible Flows and Thermal Fields," *Experiments in Fluids*, Vol. 38, No. 1, 2005, pp. 33–49. doi:10.1007/s00348-004-0881-4
[5] Grinstead, J. H., Finkelstein, N. D., Lempert, W. R., Miles, R. B., and Lavid, M., "Frequency-Modulated Filtered Rayleigh Scattering (FM-FRS)—A New Technique for Real-Time Velocimetry," AIAA Paper 96-0302, 1996.
[6] Jagodzinski, J., and Varghese, P. L., "A Diode Laser Based Velocimeter for Measurements in Unseeded Flows and Flames," AIAA Paper 2003-405, 2003.
[7] Bonnet, J. P., Grésillon, D., Cabrit, B., and Frolov, V., "Collective Light Scattering as Non-Particle Laser Velocimetry," *Measurement Science and Technology*, Vol. 6, No. 6, 1995, pp. 620–636. doi:10.1088/0957-0233/6/6/002
[8] Koochesfahani, M. M., "Molecular Tagging Velocimetry (MTV): Progress and Applications," AIAA Paper 99-3786, 1999.
[9] Liu, X., Jeffries, J. B., Hanson, R. K., Hinckley, K. M., and Woodmansee, M. A., "Development of a Tunable Diode Laser Sensor for Measurements of Gas Turbine Exhaust Temperature," *Applied Physics B (Lasers and Optics)*, Vol. 82, No. 3, 2006, pp. 469–478. doi:10.1007/s00340-005-2078-9
[10] Tropea, C., "Laser Doppler Anemometry: Recent Developments and Future Challenges," *Measurement Science and Technology*, Vol. 6, No. 6, 1995, pp. 605–619. doi:10.1088/0957-0233/6/6/001
[11] Wernet, M. P., "Temporally Resolved PIV for Space-Time Correlations in Both Cold and Hot Jet Flows," *Measurement Science and Technology*, Vol. 18, No. 5, 2007, pp. 1387–1403. doi:10.1088/0957-0233/18/5/027
[12] Samimy, M., and Wernet, M. P., "Review of Planar Multiple-Component Velocimetry in High-Speed Flows," *AIAA Journal*, Vol. 38, No. 4, 2000, pp. 553–574. doi:10.2514/2.1004
[13] Wang, G. H., Clemens, N. T., Varghese, P. L., and Barlow, R. S., "Turbulent Time Scales in A Nonpremixed Turbulent Jet Flame by Using High-Repetition Rate Thermometry," *Combustion and Flame*, Vol. 152, No. 3, 2008, pp. 317–335. doi:10.1016/j.combustflame.2007.08.010
[14] Lock, J. A., Seasholtz, R. G., and John, W. T., "Rayleigh–Brillouin Scattering to Determine One-Dimensional Temperature and Number Density Profiles of a Gas Flow Field," *Applied Optics*, Vol. 31, No. 15, 1992, pp. 2839–2848.
[15] Seasholtz, R. G., and Greer, L. C., "Rayleigh Scattering Diagnostic for Measurement of Temperature and Velocity in Harsh Environments," AIAA Paper 98-0206, 1998.
[16] Panda, J., and Seasholtz, R. G., "Velocity and Temperature Measurement in Supersonic Free Jets Using Spectrally Resolved Rayleigh Scattering," AIAA Paper 99-0296, 1999.
[17] Mielke, A. F., Seasholtz, R. G., Elam, K. A., and Panda, J., "Time-Average Measurement of Velocity, Density, Temperature, and Turbulence Velocity Fluctuations Using Rayleigh and Mie Scattering," *Experiments in Fluids*, Vol. 39, No. 2, 2005, 441–454. doi:10.1007/s00348-005-0990-8
[18] Seasholtz, R. G., and Panda, J., "Rayleigh Scattering Diagnostic for Dynamic Measurement of Velocity and Temperature," AIAA Paper 99-0641, 1999.
[19] Seasholtz, R. G., Panda, J., and Elam, K. A., "Rayleigh Scattering Diagnostic for Measurement of Velocity and Density Fluctuation Spectra," AIAA Paper 2002-0827, 2002.
[20] Bivolaru, D., Lee, J. W., Jones, S. B., Tedder, S., Danehy, P. M., Weikl, M. C., Magnotti, G., and Cutler, A. D., "Mobile CARS-IRS Instrument for Simultaneous Spectroscopic Measurement of Multiple Properties in Gaseous Flows," *22nd International Congress on Instrumentation in Aerospace Simulation Facilities*, Vol. 1, Inst. of Electrical and Electronics Engineers, Piscataway, NJ, 2007, pp. 1–9.
[21] Mielke, A. F., Elam, K. A., and Sung, C. J., "Development of a Rayleigh Scattering Diagnostic for Time-Resolved Gas Phase Flow Velocity, Temperature, and Density Measurements in Aerodynamic Test Facilities," *22nd International Congress on Instrumentation in Aerospace Simulation Facilities*, Vol. 1, Inst. of Electrical and Electronics Engineers, Piscataway, NJ, 2007, pp. 1–15.
[22] Panda, J., Seasholtz, R. G., Elam, K. A., Mielke, A. F., and Eck, D. G., "Effect of Heating on Turbulent Density Fluctuations and Noise Generation from High Speed Jets," AIAA Paper 2004-3016, 2004.
[23] Tenti, G., Boley, C., D., and Desai, R. C., "On the Kinetic Model Description of Rayleigh–Brillouin Scattering from Molecular Gases," *Canadian Journal of Physics*, Vol. 52, No. 4, 1974, pp. 285–290.
[24] Miles, R. B., Lempert, W. R., and Forkey, J. N., "Laser Rayleigh Scattering," *Measurement Science and Technology*, Vol. 12, No. 5, 2001, pp. R33–R51. doi:10.1088/0957-0233/12/5/201
[25] Boley, C. D., Desai, R. C., and Tenti, G., "Kinetic Models and Brillouin Scattering in a Molecular Gas," *Canadian Journal of Physics*, Vol. 50, No. 18, 1972, pp. 2158–2173.
[26] Vaughan, J. M., *The Fabry–Perot Interferometer, History, Theory, Practice, and Applications*, Adam Hilger, Philadelphia, 1989, pp. 89–134.
[27] Whalen, A. D., *Detection of Signals in Noise*, Academic Press, New York, 1971, pp. 327–332.
[28] Mielke, A. F., "Development of a Molecular Rayleigh Scattering Diagnostic for Simultaneous Time-Resolved Measurement of Temperature, Velocity, and Density," Ph.D. Dissertation, Dept. of Mechanical and Aerospace Engineering, Case Western Reserve Univ., Cleveland, OH, 2008.
[29] Mielke, A. F., Elam, K. A., and Sung, C. J., "Time-Resolved Rayleigh Scattering Measurements in Hot Gas Flows," AIAA Paper 2008-262, 2008.
[30] Ames Research Staff, "Equations, Tables, and Charts for Compressible Flow," NACA Rept. 1135, 1953, p. 15.
[31] Welch, P. D., "The Use of Fast Fourier Transform for the Estimation of Power Spectra: A Method Based on Time Averaging Over, Short Modified Periodograms," *IEEE Transactions on Audio and Electroacoustics*, Vol. 15, No. 2, 1967, pp. 70–73. doi:10.1109/TAU.1967.1161901
[32] Panda, J., and Seasholtz, R. G., "Experimental Investigation of Density Fluctuations in High-Speed Jets and Correlation with Generated Noise," *Journal of Fluid Mechanics*, Vol. 450, No. 1, 2002, pp. 97–130. 10.1017/S002211200100622Xdoi:
[33] Khavaran, A., and Kenzakowski, D. C., "Noise Predictions in Hot Jets," AIAA Paper 2007-3640, 2007.
[34] Khavaran, A., and Kenzakowski, D. C., "Progress Toward Improving Jet Noise Predictions in Hot Jets," AIAA Paper 2007-0012, 2007.

N. Clemens
Associate Editor